JAAS

ROYAL SOCIETY OF CHEMISTRY

PAPER

View Article Online
View Journal | View Issue

Cite this: *J. Anal. At. Spectrom.*, 2024, **39**, 2330

Investigating the effects of laser wavelengths and other ablation parameters on the detection of biogenic elements and contaminants in hydroxyapatite

Aida Fazlić, †[a] Anna Faruzelová, †[a] Jakub Buday, [ab] Lenka Michlovská,[a] Lucy Vojtová,[a] Pavlína Modlitbová, [a] Pavel Pořízka *[ab] and Jozef Kaiser [ab]

The main purpose of this work is to thoroughly describe sensitivity and resolution enhancement by systematically optimizing key parameters in laser-induced breakdown spectroscopy analysis. Simultaneous analysis of biogenic (C, P, Mg, and Ca) and contaminating (Pb) elements, which are commonly detected in selected biotic matrices (mammal teeth), was performed. Hydroxyapatite reference pellets were utilized as model matrices, which successfully reflect human dental tissue. The optimization involved precise adjustments of the used laser wavelengths (1064, 532, and 266 nm), relative defocus of the laser pulse, ablation pulse energies, and gate delays for collecting characteristic spectra. In addition, for Ca analysis, the signals of different ionization line types (Ca I 364.44 nm; Ca II 370.60 and 396.85 nm) were compared; in the case of Pb analysis, the limits of detection were established for each used laser wavelength, and the revealed differences were discussed in detail. We intend to demonstrate the benefits of rapid, low-cost analysis and also the importance of measurement parameters used in biotic sample testing.

Received 4th March 2024
Accepted 15th July 2024

DOI: 10.1039/d4ja00073k

rsc.li/jaas

Introduction

Laser-induced breakdown spectroscopy (LIBS) is an influential spectroscopic technique that enables highly effective multi-elemental detection. Its versatility is demonstrated by the combined capabilities for quantitative and qualitative analysis, while requiring minimal sample preparation. The most important advantages of LIBS are its ability to detect any chemical element, almost real-time analysis, and robust instrumentation, which enable LIBS to be deployed *in situ* with no or minimal sample preparation.[1] Other notable advantages include speed and simultaneous multiple-element analysis capabilities.[2]

In biomedical research, LIBS has solidified its position as a valuable tool for analyses of plants,[3–6] immunochemical samples,[7–10] and soft[8,11–14] and hard tissues.[15–18] Its benefits extend to the cross-sectional observation of samples and the preservation of samples after extraction from biological organisms.[19–23] In hard tissue analysis, it has been particularly applied for elemental content assessment in bones,[24,25] teeth,[15,26] other calcified tissues,[27,28] and artificially prepared hydroxyapatite standards.[29–31]

Furthermore, LIBS has proven to be a powerful tool for identifying not only biogenic elements but also contaminants, such as heavy metals (Pb, Cd, and As) in smokers' teeth.[32] This makes this method an important tool in modern human health toxicology studies.[33] In addition, it detects differences in mineral composition between healthy and contaminated tissues.[15,34,35] This technique demonstrates substantial reproducibility and efficacy in detecting heavy metals in dental samples. In particular, multiple published studies suggest that heavy metals (Hg, Ag, Sn, and Cu) from dental amalgam fillings can migrate to healthy surrounding tissues in teeth, underscoring the urgent need for an effective biomedical tool to detect heavy metals.[36,37]

In a study by Wang *et al.*,[38] a comparison of 1064 and 266 nm laser wavelengths highlighted the superior performance of the 1064 nm laser in efficiently heating the generated plasma plume and enhancing its emission. This is particularly evident in the signal-to-peak-to-noise ratio for carbon emission compared to the 266 nm laser. The more efficient heating and increased spectral intensity with the NIR laser, compared to the UV laser, are attributed to the absorption of light in the plasma, which is scaled with the square of the wavelength. Regarding plasma generation, the dependence on the material is lower for UV laser excitation than for NIR laser excitation.

[a]*CEITEC Brno University of Technology, Purkyňova 656/123, 61200 Brno, Czech Republic. E-mail: Pavel.Porizka@ceitec.vutbr.cz*

[b]*Faculty of Mechanical Engineering, Brno University of Technology, Technická 2896/2, 61669 Brno, Czech Republic*

† These authors contributed equally.

To optimize the speed and reliability of LIBS analysis for each element, critical variables such as the ablation laser wavelength and its energy per pulse, as well as additional measurement parameters – gate delay, exposure time, and laser pulse defocus – have a significant impact on the detected signal.[39]

The gate delay (GD) is another significant parameter influencing LIBS analysis. The characteristic parameters of the plasma plume, such as its spectral intensity, temperature, or electron density, are highly dependent on its evolution in time and its lifetime. The initial phase of the plasma plume is characterized by its strong continuous emission, causing certain drawbacks in the analysis. This is followed by a cooling phase, where the radiation of specific elements is more dominant. Hence, a proper selection of the collection window relative to the plasma plume evolution can be a crucial parameter in the experiment.[40]

Positive and negative defocus positions describe whether the sample is closer or farther away from the lens relative to the focal plane for the specific laser wavelength. Both positive (+) and negative (−) defocus positions significantly affect the ablation process and the amount of ablated mass, changing the plasma plume's morphology and, therefore, the spectral intensity.[19] Laser energy per pulse is another critical factor, with higher values typically resulting in a stronger spectral signal.[41] Energy and defocus together influence the ablation crater, which, in turn, affects the irradiance.[42]

In LIBS analysis, spectral intensities depend on experimental parameters, but it is also important to consider the physical and mechanical properties of the sample. Prochazka *et al.*[43] investigated optimal parameters by exploring different combinations of experimental parameters for a selected spectral line and matrix. The samples were low-alloy steel, glass, and aluminum alloy, each with different properties. An artificial neural network (ANN) model was trained using 2079 combinations of laser energies and gate delays. It was found that at least 20 initial combinations were required for training. Subsequently, only 10 experimental parameter combinations were sufficient for accurate predictions when new matrices were introduced. Optimal parameters were chosen for the highest signal-to-noise ratio (SNR), while taking into account the influence of the matrix.

This article goes beyond traditional LIBS and signal comparison methods applied to biogenic elements in hard tissues. We emphasize the importance of heavy metals, optimizing parameters for both biogenic and contaminating elements, while comparing three ablation laser wavelengths. A careful comparison of different wavelengths under consistent experimental conditions is crucial. Previous studies have often optimized only one or two wavelengths using different lasers, which may influence the results. To overcome this, a systematic investigation of fundamental and harmonic wavelengths from a single laser source with changeable harmonic wavelengths is important. This provides more reliable and extensive information to help interpret the experimental results. In addition, the study includes a comparative analysis of atomic and ionic perspectives, exploring the influence of LIBS parameters on this comprehensive investigation.

Materials and methods

Preparation of calibration samples

Because of ethical reasons associated with animal or human teeth sample recovery, specially prepared reference samples were used in this study. Produced from a similar matrix to real teeth (calcium-deficient hydroxyapatite, $Ca_9(HPO_4)(PO_4)_6OH$), these reference samples had previously shown great potential as an accurate alternative to real dental samples.[29–31]

A set of 60 phosphate-based standards prepared according to Vojtová *et al.*[44] pressed into pellets with a diameter of 5 mm and a thickness of 1.5 mm was prepared. To briefly summarize, samples were prepared by mixing Pluronic® F-127 aqueous solution with lead (liquid phase) and tricalcium phosphate (powder phase) with a liquid to powder phase ratio of 0.5 g g^{-1}. The prepared matrix was dosed into silicone molds with dimensions 5 × 2 mm, and samples were hardened at 37 °C for 3 days when tricalcium phosphate was transformed into calcium-deficient hydroxyapatite. All samples were loaded with predefined amounts of lead (Pb). Initially, a range of Pb concentrations (in the form of $PbCl_2$) from 100 to 1000 ppm (steps of 100 ppm) was investigated for sufficient Pb amount determination for further optimization. Based on the calculation of the LOD and the characteristics of the spectra in this range, we selected a concentration of 400 ppm for the rest of the sample set to be used in the subsequent parameters' optimization. Furthermore, their precise concentration was cross-checked by Inductively Coupled Plasma Optical Emission Spectroscopy (ICP-OES) as a reference method (data shown in Table 1).

LIBS measurement system

The experiments were performed on a FireFly LIBS system (Lightigo, Czech Republic) equipped with a Nd:YAG ablation laser with fundamental 1064 nm (~6 ns) and harmonics 532 nm (~6 ns) and 266 nm (~8 ns) wavelengths. All measurements were carried out in an argon purge of high purity (99.996%) with a flow rate maintained at 9 L min^{-1}. For spectral analysis, two Czerny–Turner spectrometers were used, hereafter referred to as SP1 and SP2. Spectrometer SP1 (range 245–410 nm and gate width 50 μm) equipped with an embedded CMOS detector was used for the acquisition of wide-range spectra and detection of biogenic elements. Simultaneously, we employed spectrometer

Table 1 Average concentrations of lead in phosphate-based standards obtained by ICP-OES

Sample	c_{Pb} (ppm)	SD (ppm)
1	377	3
2	384	7
3	382	6
4	393	3
5	385	5

SP2 (central wavelength 405 nm, spectral range 25 nm, and gate width 50 μm) coupled with a sCMOS detector for more sensitive results in detecting the contaminating element (Pb). An optical apochromatic triplet lens designed for the use of all three ablation laser wavelengths with a focal length of $f = 35$ mm was employed. The repetition rate was 1 Hz for each measurement.

Experimental parameters

A grid of 5 × 5 maps was measured, employing a single-shot mode, ensuring that each spot received only one laser pulse without accumulation and resulting in 25 spectra per combination of the parameters. To prevent the overlapping of the ablation craters, a step size of 250 μm was utilized, considering the variability in ablation crater sizes ranging from approximately 100 to 200 μm. In the case of 1064 nm and 532 nm laser wavelengths, five laser pulse energies were optimized, adjusting the defocus settings and gate delays of the spectrometers in five different configurations, resulting in 125 different combinations per laser wavelength. On the other hand, for the 266 nm laser wavelength, the pulse energies were limited to four due to a noticeable decrease in spectral intensities for lower pulse energies, resulting in 100 different configurations. By adjusting the energy per pulse and its relative defocus, we directly influenced the ablation crater and, consequently, possible resolution. The radius of the ablation crater was used to calculate another parameter – irradiance. The range of the optimized gate delay values was derived from the lifetime and the spectral intensity of the plasma plume, as well as from the intensity of the continuous radiation. This is increased in the earlier stages of the plasma plume lifetime with the increasing wavelength of the ablation laser.[1] Hence, for UV ablation, the values are lowest near the ablation event, but increase for the other laser wavelengths. Positive defocus of the laser pulse means that the distance between the lens and the analyzed sample is greater than the focal length, while negative defocus indicates that the distance is less than the focal length (laser-focused below the sample surface). No spectra correction was performed prior to any data evaluation. The signal dependence was calculated as a correlation with gate delay and irradiance. Table 2 displays the varied parameters selected for each laser wavelength, while Table 3 illustrates the calculated irradiance for each corresponding laser wavelength. As mentioned above, this study's focus was on the optimization of ablation parameters for biogenic elements, with selected elements and emission lines mentioned in Table 4. Additionally, a comparison of the optimal parameters for the detection of atomic and ionic lines was explored on the calcium lines Ca I 364.44 nm and Ca II 370.60 nm. Lastly, we aimed to determine the optimal parameters for contaminating element detection by focusing on lead Pb I 407.78 nm analysis.

Table 3 Calculated irradiance for each laser wavelength

Laser wavelength (nm)	Irradiance (GW cm^{-2})
266	5.1, 5.3, 5.4, 5.5, 5.6, 6.3, 6.5, 6.6, 6.9, 7.0, 7.1, 7.4, 7.5, 7.6, 7.7, 7.8, 7.9, 8.2, 8.3, 8.6
532	12.8, 13.2, 13.5, 14.9, 15.7, 18.7, 19.4, 19.9, 21.4, 24.1, 25.3, 25.6, 28.3, 28.5, 31.8, 32.5, 32.6, 33.1, 36.0, 37.8, 38.4, 39.3, 40.1, 47.3, 52.3
1064	12.8, 12.9, 13.8, 14.5, 17.1, 18.9, 19.0, 20.0, 22.3, 22.6, 26.1, 28.8, 29.8, 30.0, 30.5, 34.4, 35.3, 36.0, 38.5, 38.8, 39.1, 40.8, 42.9, 44.7, 48.6

Table 4 List of analyzed spectral lines and their properties – spectral line (λ), Einstein coefficient (A_{ki}), and lower (E_i) and upper (E_k) energy levels.[45]

Spectral line	λ (nm)	A_{ki} ($\times 10^8$ s^{-1})	E_i (eV)	E_k (eV)	Spectrometer
C I	247.86	2.80	2.68	7.69	SP1
P I	253.56	0.95	2.32	7.21	
Mg II	279.55	2.60	0.00	4.43	
Ca I	364.44	0.35	1.90	5.30	
Ca II	370.60	0.88	3.12	6.47	
Ca II	396.85	1.40	0.00	3.12	SP2
Pb I	405.78	1.32	4.38	9.00	

Examples of the captured spectra from both used spectrometers and the specific spectral lines of interest are shown in Fig. 1.

The overall goal of this research was to identify optimal parameters for the mentioned elements, highlighting differences between different elements and states. This was accomplished by prioritizing the highest signal-to-background ratio (SBR) and optimal resolution. However, in the case of Pb, an additional factor considered was the limit of detection (LOD), which was calculated using the formula:

$$\mathrm{LOD} = \frac{3c\mathrm{SD}}{\overline{X_{\mathrm{Pb}}}} \quad (1)$$

where c denotes the element's concentration, and SD stands for the background's standard deviation, which is multiplied by three to obtain 99% of the reference sample's results. $\overline{X_{\mathrm{Pb}}}$ refers to the average element response due to the signal and background.[46]

Table 2 Optimization of parameters for 266 nm, 532 nm, and 1064 nm ablation laser wavelengths

Laser wavelength (nm)	Pulse energy (mJ)	Gate delay (μs)	Relative defocus (mm)
266	7, 8, 9, 10	0.1, 0.3, 0.5, 0.7, 0.9	−1.0, −0.5, 0.0, 0.5, 1.0
532	20, 30, 40, 50, 60	0.50, 1.00, 1.25, 1.50, 1.75	−1.0, −0.5, 0.0, 0.5, 1.0
1064	20, 30, 40, 50, 60	1, 2, 3, 4, 5	−1.0, −0.5, 0.0, 0.5, 1.0

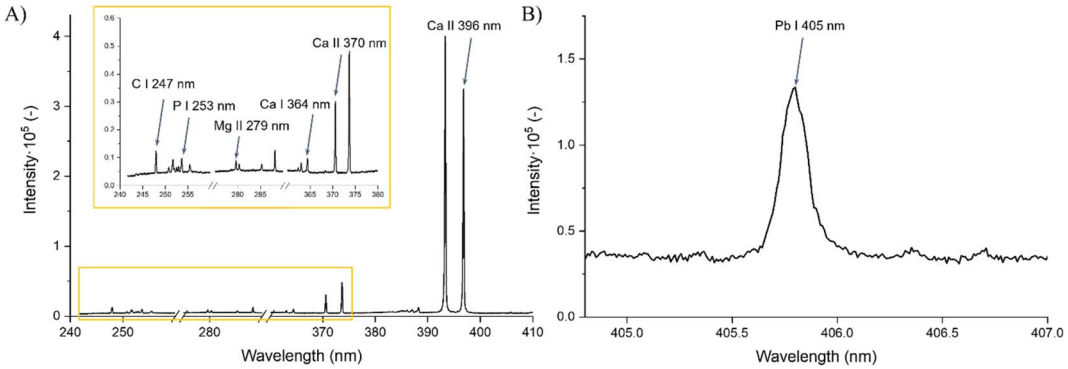

Fig. 1 Spectra obtained from (A) SP1 with marked spectral lines of biogenic elements and (B) SP2 showing the detected line Pb I 405.78 nm. Both shown spectra were acquired from a measurement with a laser wavelength of 1064 nm, pulse energy of 60 mJ, relative defocus of 0 mm, and gate delay of 5 μs.

Results and discussion

Biogenic elements

In the evaluation of the SBR for Mg, the highest SBR value, 3.370, was achieved using a 1064 nm laser wavelength. Optimal SBR results were obtained with increased irradiances and low gate delays. On the other hand, when using a 532 nm laser wavelength, the gate delay had a small effect on the SBR, with higher irradiances providing consistently better results. Notably, there was no apparent trend in SBR values when using a 266 nm laser wavelength.

In the detection of P, across all laser wavelengths, higher irradiances consistently yielded a higher SBR (Fig. 2). This trend was similarly observed for C. The highest signals for P and C were

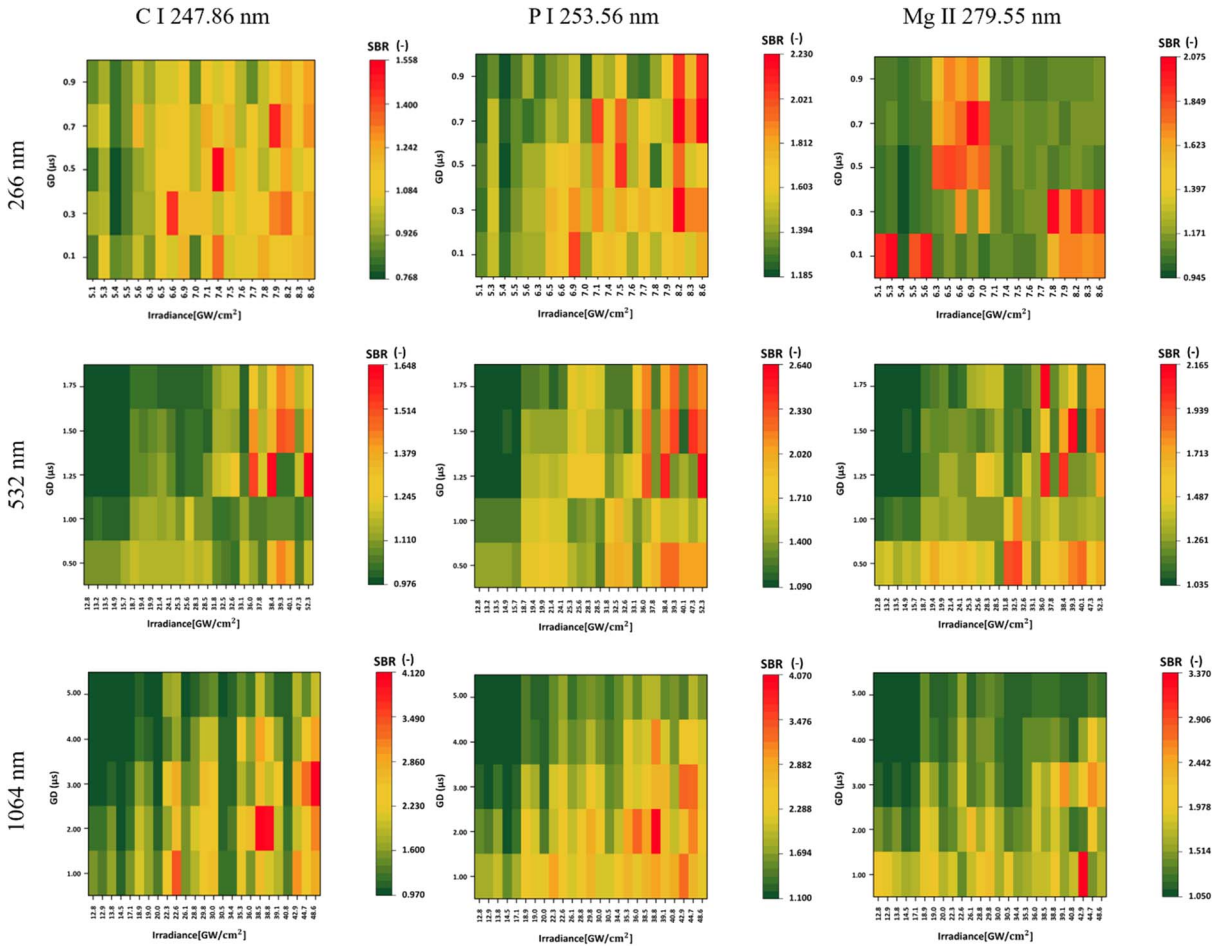

Fig. 2 Dependence of the SBR on irradiance and gate delay for 266, 532, and 1064 nm laser wavelengths shown by heatmaps for selected spectral lines of C I 247.86 nm, P I 253.56 nm, and Mg II 279.80 nm calculated from spectra obtained using SP1.

obtained with a 1064 nm laser, measuring 4.070 and 4.120, respectively. Notably, the difference between different lasers is evident, as the SBR is much higher when measuring with a 1064 nm laser compared to 266 nm for P, as illustrated in Fig. 2.

As highlighted in the Introduction, this study delved into the observation of different ionic states, particularly in the comparison of Ca I and Ca II. While higher gate delays correlated with a higher SBR for the atomic line, the opposite trend was observed for the ionic line, where stronger signals were typical for lower gate delays. This is based on the lifetime behavior of different ionic stages based on the plasma plume temperature and expansion behaviors. Higher laser irradiances proved to be more effective in the excitation of both atomic and ionic lines. However, an increase in laser irradiance, or the laser wavelength, generally leads to an increase in the continuous emission of the plasma plume. Hence, it is important to keep this in mind when focusing the analysis on specific spectral lines with relatively weaker signals that can be surpassed by this emission. However, an increase in the SBR was observed in all instances when a higher laser wavelength was applied for the ablation. Specifically, the SBR values for Ca I obtained from laser wavelengths 1064, 532, and 266 nm were 4.470, 3.530, and 2.650, respectively. Similarly, the corresponding SBR values for Ca II were 7.120, 5.580, and 3.440. All of the findings are illustrated in Fig. 3.

For UV ablation, the plasma plume is small and compact, with higher temperatures, a relatively short lifetime, and negligible continuous radiation. Therefore, the ionic line

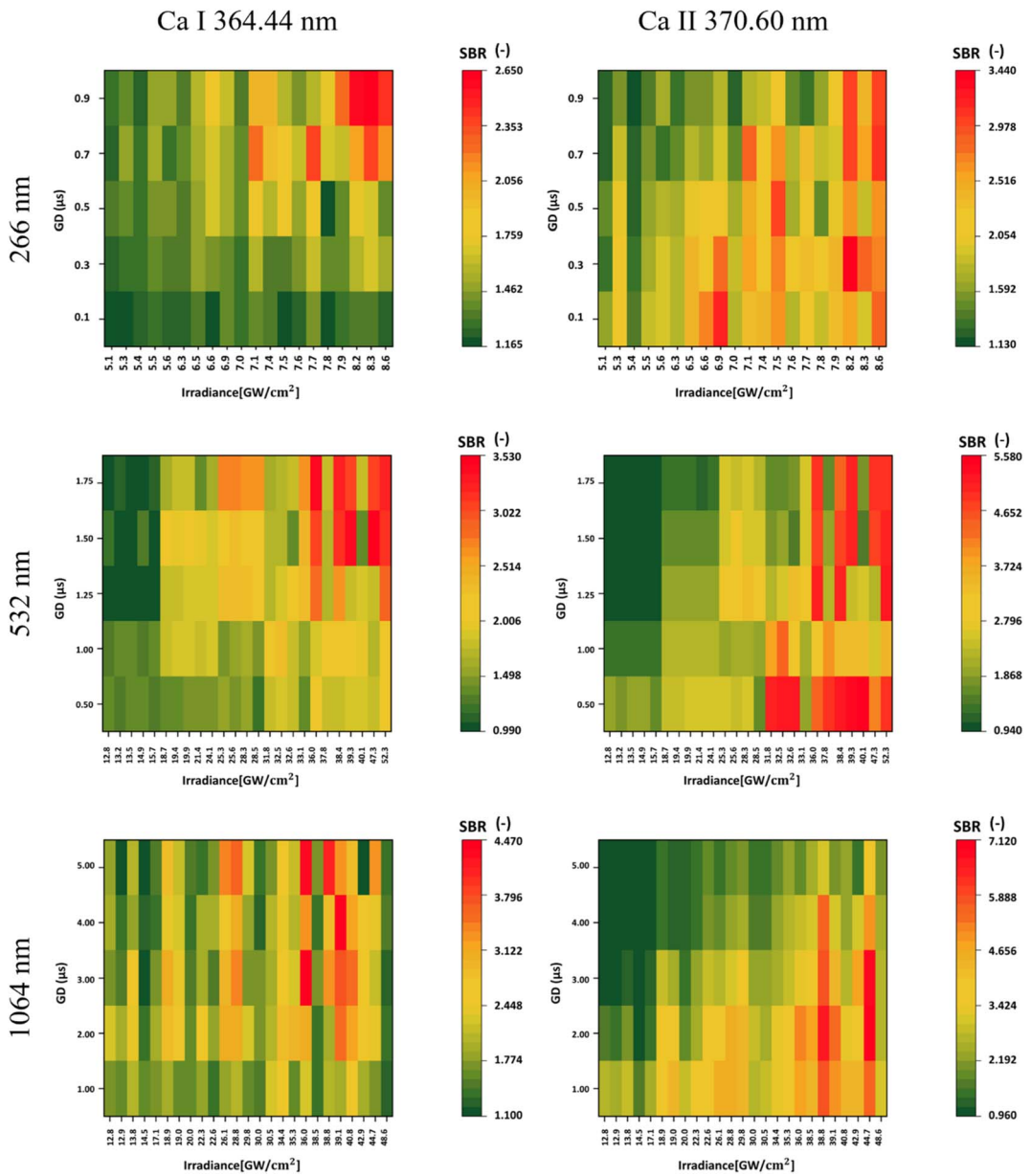

Fig. 3 Dependence of the SBR on irradiance and gate delay for 266, 532, and 1064 nm laser wavelengths shown by heatmaps for calcium atomic Ca I 364.44 nm and ionic Ca II 370.60 nm lines calculated from spectra obtained using SP1.

radiation is strong from the beginning of the plasma plume's lifetime, even for lower irradiance values compared to both 1064 and 532 laser ablation. However, the lifetime of the ionic stages is relatively shorter. In the IR, plasma shielding occurs, where part of the laser pulse is absorbed in the shocked gas layer. Here, the temperature of the plasma plume is higher, with a longer lifetime, and hence, the conditions for the presence of Ca ions are longer. This results in a strong emission signal even in the later stages of the plasma plume, when the temperature is still high enough and the strong continuum is no longer present. For the 532 nm laser wavelength, plasma shielding may still occur, but the lifetime and temperature of the plasma plume are reduced compared to the IR ablation, so the radiation also starts to decrease in the later stages.[47,48]

Our results showed a higher SBR during ablation with a longer laser wavelength. These results are in line with the publication of M.A. Kasem *et al.*,[49] who studied archaeological bone samples using LIBS. However, it should be noted that their study used two different laser systems for two ablation laser wavelengths, UV and IR, whereas we used a single system to compare all three laser wavelengths. Therefore, the compared stability of the signals and the plasma plume, which was also observed and discussed, can be partially attributed to the different properties of the two lasers. In addition, they did not include a 532 nm ablation laser in the analysis. Moreover, they investigated the ionic-to-atomic line ratio of calcium (Ca II/Ca I) for both laser wavelengths. Our results are in agreement with theirs since they observed a reduced signal intensity in UV-LIBS, together with faster plasma decay.

In contrast to our results, Xiongwei L. *et al.*[50] observed higher C signal intensities at the 266 nm laser wavelength. This difference may be due to their use of a uniform 40 mJ pulse energy for both 266 nm and 1064 nm wavelengths. Their investigation, focusing on coal samples and ours on hydroxyapatite standards, highlights the significant influence of the sample matrix on the selection of an optimal laser wavelength. In particular, their selection of the 266 nm wavelength laser resulted not only in increased C signal intensities but also in improved reproducibility. These improvements were associated with the reduction of thermal effects and plasma shielding compared to the 1064 nm laser wavelength, highlighting the critical role of the laser wavelength in influencing the analytical results.

Contaminant detection

In the context of Pb detection, within the measurements performed with a 266 nm laser, the highest SBR was obtained using the highest combination of irradiance and gate delay. Specifically, for Pb, we calculated the LOD since the samples had a known concentration of Pb. Optimal results for the laser wavelengths 266 nm, 532 nm, and 1064 nm gave LODs of 226.22, 251.84, and 135.20 ppm, respectively. The highest SBR achieved with the UV laser was 1.474, while for 532 nm, it was 1.528, and for 1064 nm, it reached 2.640. Hence, the highest laser wavelength not only yielded the best signal intensities but also achieved the lowest LODs among the three wavelengths.

Optimal results with a 532 nm laser were achieved by using lower irradiances and higher gate delays for Pb detection. Conversely, when using 266 nm and 1064 nm lasers for measurements, better results were obtained with higher gate delays and irradiances.

Since Pb I represents an atomic state, a comparison was made with Ca II (ionic state) using the emission line obtained using SP2 at 396.85 nm. In this case, higher gate delays resulted in a higher SBR for both elements from 266 and 1064 nm laser wavelength measurements. However, for Ca, lower irradiances resulted in a higher SBR, while the opposite was observed for Pb. For the 532 nm laser wavelength, lower irradiances resulted in a higher SBR for both elements. However, while detecting Pb, higher gate delays should be used. Even for Ca, the highest SBR was achieved at higher laser wavelengths, reaching 2.640, 1.528, and 1.474 for 1064 nm, 532 nm, and 266 nm, respectively.

When comparing Ca II 396.85 nm and Ca II 370.60 nm, an opposite trend was observed, even though both of these emission lines are in an ionic state. This is caused by the self-absorption of the 396.85 nm line, where the signal of the spectral line shows only a minimal increase in its intensity with

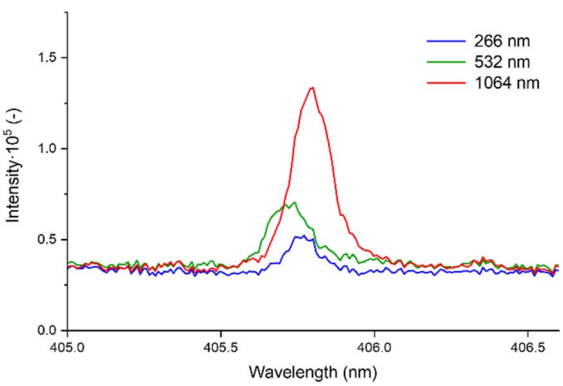

Fig. 4 Comparative analysis of signal intensities for Pb I 405.78 nm detection from all laser wavelengths acquired with optimal parameters from Table 5.

Table 5 Optimal results for each laser wavelength and configuration for SP-LIBS for Pb detection with the best possible parameters highlighted (in bold)

Laser wavelength (nm)	E (mJ)	def (mm)	GD (μs)	Spot size (mm)	I_e (GW cm^{-2})	SBR (–)	LOD (ppm)	SD (–)	RSD (%)
266	9	0.5	0.70	0.16	7.81	1.26	226.22	0.09	7.3
532	30	1.0	1.75	0.17	18.67	1.52	251.84	0.12	7.7
1064	60	0.0	5.00	0.16	48.54	2.57	135.20	0.30	12.6

higher irradiance, while the increase in continuous background emission is more dominant. Hence, the SBR values are lower for higher irradiance.

The best set of parameters was then evaluated not only on the basis of the SBR but also taking into account the effect of the ablation crater on the resolution and LOD. Of the three laser wavelengths, 1064 nm gave the best results, with a LOD of 135.20 ppm, an SBR of 2.57, and a spot size of 0.16 mm.

The most optimized results were also found to be acquired for each wavelength when the laser was focused below the sample surface (0.5 mm for the 266 nm laser wavelength and 1.0 mm for the 532 nm laser wavelength) or precisely on the sample (0.0 mm for the 1064 nm laser wavelength).

In Table 5, we present the selection of optimal outcomes for each laser wavelength, encompassing the calculated LOD and the measured ablation craters, which influence the resolution. Fig. 4 comprehensively compares three distinct laser wavelengths, showcasing results derived from the identified optimal parameters. Additionally, Fig. 5 showcases heatmaps displaying all results for every parameter combination across all ablation laser wavelengths.

Our research shares a similar objective with the study conducted by O. Samek *et al.*, who also focused on detecting trace metals in teeth using LIBS.[51] While Samek *et al.* focused primarily on trace element analysis in teeth, they did not investigate the effect of varying laser wavelengths and

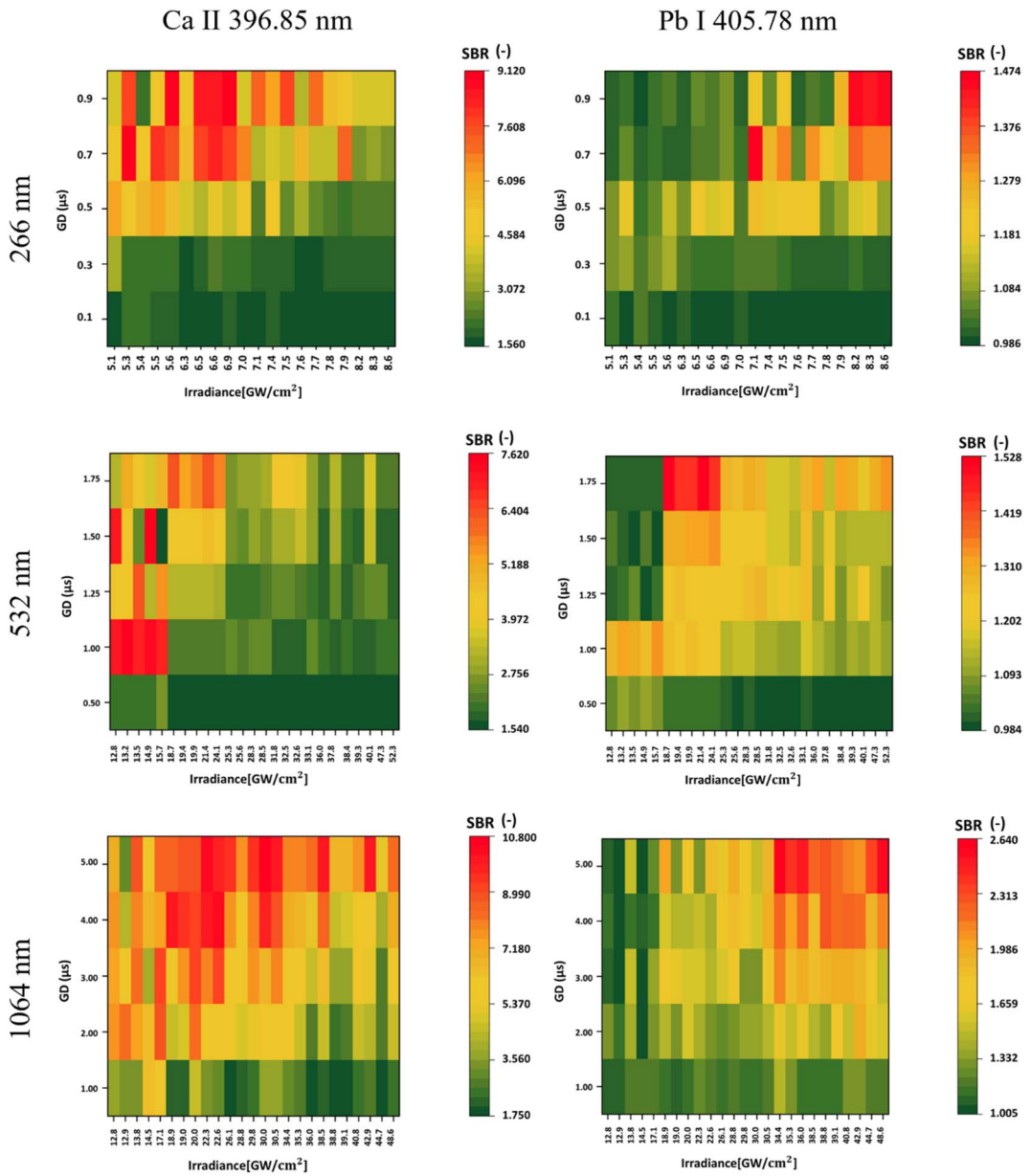

Fig. 5 Dependence of the SBR on irradiance and gate delay for 266, 532, and 1064 nm laser wavelengths for Pb I 405.78 nm and Ca II 396.85 nm shown by heatmap calculated from spectra obtained using SP2.

parameters. Nevertheless, their work, like ours, establishes LIBS as a viable method for the detection of contaminants. In teeth, metals, such as Ti, were absorbed from toothpaste and fillings. Similarly, in a study by Hawraa J. N. *et al.*,[52] LIBS was used to analyze heavy metals in gallstones using a laser wavelength of 1064 nm. Calibration curves were established for Cr, Cd, Zn, Pb, Cu, and As, and various gallstone samples were compared. The study concluded that heavy metals, including Pb, are present in gallstones from smoking patients, providing valuable insights into contaminant detection. These studies highlight the versatility and effectiveness of LIBS in detecting contaminants in various materials.

Conclusion

This study focuses on the impact of experimental parameters on the spectral intensity of selected spectral lines, specifically laser irradiance (changed by varying its pulse energy or relative defocus) and gate delay during spectra acquisition. These parameters play a critical role in the detection of biogenic and contaminating elements within the hydroxyapatite matrix simulating dental tissues. Specifically, for magnesium detection, variations in laser wavelengths produced the following trends: no specific pattern emerged for the 266 nm laser; a higher SBR was achieved at higher irradiances in general for the 532 nm laser; optimal results were observed at lower gate delays and higher irradiance for the 1064 nm laser. Similarly, phosphorus and carbon detection showed a consistent correlation between higher irradiances and increased SBRs across all laser wavelengths, with the 1064 nm laser providing the highest signals for both elements. In addition, the study of Ca I and Ca II revealed interesting relationships: higher gate delays correlated with higher SBRs for Ca I, while the opposite was true for Ca II, with higher irradiances proving more effective for both states and higher laser wavelengths resulting in increased SBR values.

For the detection of Pb, the optimal SBR was achieved with a 1064 nm laser using the maximum irradiance and gate delay, while for a 532 nm laser, optimal results were found with lower irradiances and higher gate delays. LOD assessments were conducted for Pb. The 1064 nm laser wavelength produced the highest SBR and the lowest LOD, with values of 2.57 and 135.20 ppm, respectively. A comparative analysis between Pb I (atomic state) and Ca II (ionic state) highlighted different trends in gate delays and irradiances depending on different laser wavelengths.

Data availability

Data for this article are available at **https://doi.org/10.5281/zenodo.11635995**.

Author contributions

Aida Fazlić: spectroscopic analysis, data processing, visualization, writing – original draft, and writing – review and editing; Anna Faruzelová: conceptualization, data processing, visualization, writing – original draft, and writing – review and editing; Jakub Buday: conceptualization, methodology, and writing – original draft; Lenka Michlovská: sample preparation; Lucy Vojtová: sample design and funding; Pavlína Modlitbová: writing – review and editing; Pavel Pořízka: supervision, writing – review and editing, and funding; Jozef Kaiser: supervision and funding.

Conflicts of interest

There are no conflicts to declare.

Acknowledgements

The authors acknowledge the support of the Czech Science Foundation (no. 23-13617L). LV acknowledges the support of the profiBONE project (TO01000309) that benefits from a € 1.433.000 grant from Iceland, Liechtenstein, and Norway through the EEA Grants and the Technology Agency of the Czech Republic. A. Faruzelova and JB acknowledge the support of the Brno University of Technology project no. CEITEC VUT/FSI-J-23-8365. A. Fazlic acknowledges the support of Infineon. JK acknowledges the support of the Faculty of Mechanical Engineering at the Brno University of Technology (no. FSI-S-23-8389).

References

1 R. Noll, *Laser-Induced Breakdown Spectroscopy*, Springer Berlin Heidelberg, Berlin, Heidelberg, 2012, available from: **https://link.springer.com/10.1007/978-3-642-20668-9**.
2 A. Limbeck, L. Brunnbauer, H. Lohninger, P. Pořízka, P. Modlitbová, J. Kaiser, *et al.*, Methodology and applications of elemental mapping by laser induced breakdown spectroscopy, *Anal. Chim. Acta*, 2021, **1147**, 72–98.
3 T. Brennecke, L. Čechová, K. Horáková, L. Šimoníková, J. Buday, D. Prochazka, *et al.*, Imaging the distribution of nutrient elements and the uptake of toxic metals in industrial hemp and white mustard with laser-induced breakdown spectroscopy, *Spectrochim. Acta Part B At. Spectrosc.*, 2023, **205**, 106684. available from: **https://linkinghub.elsevier.com/retrieve/pii/S058485472300071X**.
4 P. Modlitbová, S. Střítežská, A. Hlaváček, L. Šimoníková, K. Novotný, P. Pořízka, *et al.*, The effects of co-exposures of Zea mays plant to the photon-upconversion nanoparticles; does the size or composition play an important role?, *Spectrochim. Acta Part B At. Spectrosc.*, 2022, **197**, 106526.
5 J. Ren, Y. Zhao and K. Yu, LIBS in agriculture: A review focusing on revealing nutritional and toxic elements in soil, water, and crops, *Comput. Electron. Agric.*, 2022, **197**, 106986.
6 P. D. Ilhardt, J. R. Nuñez, E. H. Denis, J. J. Rosnow, E. J. Krogstad, R. S. Renslow, *et al.*, High-resolution elemental mapping of the root-rhizosphere-soil continuum using laser-induced breakdown spectroscopy (LIBS), *Soil Biol. Biochem.*, 2019, **131**, 119–132.

7 P. Pořízka, K. Vytisková, R. Obořilová, M. Pastucha, I. Gábriš, J. C. Brandmeier, *et al.*, Laser-induced breakdown spectroscopy as a readout method for immunocytochemistry with upconversion nanoparticles, *Microchim. Acta*, 2021, **188**(5), 1–10. available from: **https://link.springer.com/article/10.1007/s00604-021-04816-y**.

8 P. Pořízka, P. Modlitbová, N. Melikechi and J. Kaiser, Laser-ablation spectroscopy for imaging of tumor markers and nanoparticle labels, in: *Optical Spectroscopy and Imaging for Cancer Diagnostics*, World Scientific, 2023, pp. 181–206.

9 N. Melikechi and Y. Markushin, Tag-laser-induced breakdown spectroscopy with Si, Ti, and Fe micro-particles and analysis of leptin in a phosphate buffer solution, *Spectrochim. Acta Part B At. Spectrosc.*, 2022, **188**, 106357.

10 A. Safi, J. E. Landis, H. G. Adler, H. Khadem, K. E. Eseller, Y. Markushin, *et al.*, Enhancing biomarker detection sensitivity through tag-laser induced breakdown spectroscopy with NELIBS, *Talanta*, 2024, **271**, 125723.

11 P. Janovszky, A. Kéri, D. J. Palásti, L. Brunnbauer, F. Domoki, A. Limbeck, *et al.*, Quantitative elemental mapping of biological tissues by laser-induced breakdown spectroscopy using matrix recognition, *Sci. Rep.*, 2023, **13**(1), 10089.

12 J. Lin, Y. Li, X. Lin and C. Che, Fusion of laser-induced breakdown spectroscopy technology and deep learning: a new method to identify malignant and benign lung tumors with high accuracy, *Anal. Bioanal. Chem.*, 2024, **416**(4), 993–1000.

13 P. Winnand, K. O. Boernsen, G. Bodurov, M. Lammert, F. Hölzle and A. Modabber, Evaluation of electrolyte element composition in human tissue by laser-induced breakdown spectroscopy (LIBS), *Sci. Rep.*, 2022, **12**(1), 16391.

14 H. Kopřivová, K. Kiss, L. Krbal, V. Stejskal, J. Buday, P. Pořízka, *et al.*, Imaging the elemental distribution within human malignant melanomas using Laser-Induced Breakdown Spectroscopy, *Anal. Chim. Acta*, 2024, 342663.

15 P. Pořízka, A. Konečná, A. Šindelářová, M. Šulcová, P. Modlitbová, D. Prochazka, *et al.*, Feasibility of laser-induced breakdown spectroscopy to elucidate elemental changes in human tooth ankylosis, *Spectrochim. Acta Part B At. Spectrosc.*, 2023, **206**, 106727.

16 J. Lavicky, M. Kolouskova, D. Prochazka, V. Rakultsev, M. Gonzalez-Lopez, K. Steklikova, *et al.*, The Development of Dentin Microstructure Is Controlled by the Type of Adjacent Epithelium, *J. Bone Miner. Res.*, 2022, **37**(2), 323–339. available from: **https://onlinelibrary.wiley.com/doi/10.1002/jbmr.4471**.

17 B. T. Manard, C. J. Hintz, C. D. Quarles, W. Burns, N. A. Zirakparvar, D. R. Dunlap, *et al.*, Determination of fluorine distribution in shark teeth by laser-induced breakdown spectroscopy, *Metallomics*, 2022, **14**(7), mfac050.

18 S. Al-Bourgol, G. Machinet, A. Bakkali, M. Faucon and L. Gemini, Real-Time Monitoring of Thermal Phenomena during Femtosecond Ablation of Bone Tissue for Process Control, *Bioengineering*, 2024, **11**(4), 309.

19 S. J. Rehse, Biomedical Applications of LIBS, Springer, Berlin, Heidelberg, 2014, pp. 457–488.

20 V. K. Singh and A. K. Rai, Prospects for laser-induced breakdown spectroscopy for biomedical applications: a review, *Laser Med. Sci.*, 2011, **26**(5), 673–687.

21 B. Busser, S. Moncayo, J. L. Coll, L. Sancey and V. Motto-Ros, Elemental imaging using laser-induced breakdown spectroscopy: A new and promising approach for biological and medical applications, *Coord. Chem. Rev.*, 2018, **358**, 70–79.

22 V. Gardette, V. Motto-Ros, C. Alvarez-Llamas, L. Sancey, L. Duponchel and B. Busser, Laser-Induced Breakdown Spectroscopy Imaging for Material and Biomedical Applications: Recent Advances and Future Perspectives, *Anal. Chem.*, 2023, **95**(1), 49–69.

23 A. V. Skalny, T. V. Korobeinikova, M. Aschner, O. V. Baranova, E. G. Barbounis, A. Tsatsakis, *et al.*, Medical application of laser-induced breakdown spectroscopy (LIBS) for assessment of trace element and mineral in biosamples: Laboratory and clinical validity of the method, *J. Trace Elem. Med. Biol.*, 2023, **79**, 127241.

24 H. Abbasi, P. C. Cattin, G. Rauter, A. Zam, Differentiation of femur bone from surrounding soft tissue using laser-induced breakdown spectroscopy as a feedback system for smart laserosteotomy, *Biophotonics: Photonic Solutions for Better Health Care VI*, SPIE-Intl Soc Optical Eng, 2018, p. 60.

25 A. Marín Roldán, V. Dwivedi, J. Yravedra Sainz de los Terreros and P. Veis, Laser-Induced breakdown spectroscopy (LIBS) for the analyses of faunal bones: Assembling of individuals and elemental quantification, *Optik*, 2020, **218**, 164992.

26 K. F. Abdullah and S. J. Kadhem, Analysis of laser induced breakdown spectra for distinguish between healthy and carious teeth, *J. Opt.*, 2024, DOI: **10.1007/s12596-024-01791-4**.

27 S. A. Davari, S. Masjedi, Z. Ferdous and D. Mukherjee, In-vitro analysis of early calcification in aortic valvular interstitial cells using Laser-Induced Breakdown Spectroscopy (LIBS), *J. Biophot.*, 2018, **11**(1), e201600288.

28 V. K. Singh, V. Kumar and J. Sharma, Importance of laser-induced breakdown spectroscopy for hard tissues (bone, teeth) and other calcified tissue materials, *Laser Med. Sci.*, 2015, **30**(6), 1763–1778.

29 M. Martinez, C. Bayne, D. Aiello, M. Julian, R. Gaume and M. Baudelet, Multi-elemental matrix-matched calcium hydroxyapatite reference materials for laser ablation: Evaluation on teeth by laser-induced breakdown spectroscopy, *Spectrochim. Acta Part B At. Spectrosc.*, 2019, **159**, 105650.

30 M. Martinez and M. Baudelet, Calibration strategies for elemental analysis of biological samples by LA-ICP-MS and LIBS – A review, *Anal. Bioanal. Chem.*, 2020, **412**(1), 27–36.

31 G. C. Gomes, F. O. Borges, F. F. Borghi, G. H. Cavalcanti, C. M. S. Martins, V. Palleschi, *et al.*, Rapid stoichiometric analysis of calcium-phosphorus ratio on hydroxyapatite targets by one-point calibration laser-induced breakdown spectroscopy, *Spectrochim. Acta Part B At. Spectrosc.*, 2021, **184**, 106250.

32 A. M. Alhasmi, M. A. Gondal, M. M. Nasr, S. Shafik and Y. B. Habibullah, Detection of toxic elements using laser-induced breakdown spectroscopy in smokers' and nonsmokers' teeth and investigation of periodontal parameters, *Appl. Opt.*, 2015, **54**(24), 7342.

33 S. Sharma GK, Trend in the analysis of heavy metals in human teeth dentine: a review, *Indo Pac. Acad. Forensic Odontology*, 2020, (2), 93–112. available from: https://www.researchgate.net/publication/347975986_Trend_in_the_analysis_of_heavy_metals_in_human_teeth_dentine_a_review.

34 R. Gaudiuso, N. Melikechi, Z. A. Abdel-Salam, M. A. Harith, V. Palleschi, V. Motto-Ros, *et al.*, Laser-induced breakdown spectroscopy for human and animal health: A review, *Spectrochim. Acta Part B At. Spectrosc.*, 2019, **152**, 123–148.

35 P. Modlitbová, P. Pořízka and J. Kaiser, Bioimaging in Laser-Induced Breakdown Spectroscopy, in: *Laser Induced Breakdown Spectroscopy (LIBS)*, Wiley, 2023, pp. 729–744.

36 A. V. Skalny, T. V. Korobeinikova, M. Aschner, O. V. Baranova, E. G. Barbounis, A. Tsatsakis, *et al.*, Medical application of laser-induced breakdown spectroscopy (LIBS) for assessment of trace element and mineral in biosamples: Laboratory and clinical validity of the method, *J. Trace Elem. Med. Biol.*, 2023, **79**, 127241.

37 M. Gazmeh, M. Bahreini and S. H. Tavassoli, Discrimination of healthy and carious teeth using laser-induced breakdown spectroscopy and partial least square discriminant analysis, *Appl. Opt.*, 2015, **54**(1), 123.

38 Q. Wang, P. Jander, C. Fricke-Begemann and R. Noll, Comparison of 1064 nm and 266 nm excitation of laser-induced plasmas for several types of plastics and one explosive, *Spectrochim. Acta Part B At. Spectrosc.*, 2008, **63**(10), 1011–1015.

39 A. W. Miziolek, V. Palleschi and I. Schechter, *Laser-Induced Breakdown Spectroscopy (LIBS)*, ed. A. W. Miziolek, V. Palleschi, I. Schechter, Cambridge University Press, Cambridge, 2006, available from: https://www.cambridge.org/core/product/identifier/9780511541261/type/book.

40 L. C. L. Borduchi, D. M. B. P. Milori and P. R. Villas-Boas, Study of the effects of detection times in laser-induced breakdown spectroscopy and missed variation of plasma parameters with gate width, *Spectrochim. Acta Part B At. Spectrosc.*, 2022, **191**, 106409.

41 V. Lazic and M. Ciaffi, Laser-Induced Breakdown Spectroscopy Applied on Liquid Films: Effects of the Sample Thickness and the Laser Energy on the Signal Intensity and Stability, *J. Spectrosc.*, 2017, **2017**, 1–10.

42 S. Musazzi and U. Perini, *LIBS Instrumental Techniques*, 2014, pp. 59–89.

43 D. Prochazka, P. Pořízka, J. Hruška, K. Novotný, A. Hrdlička and J. Kaiser, Machine learning in laser-induced breakdown spectroscopy as a novel approach towards experimental parameter optimization, *J. Anal. At. Spectrom.*, 2022, **37**(3), 603–612.

44 L. Vojtova, L. Michlovska, K. Valova, M. Zboncak, M. Trunec, K. Castkova, *et al.*, The Effect of the Thermosensitive Biodegradable PLGA–PEG–PLGA Copolymer on the Rheological, Structural and Mechanical Properties of Thixotropic Self-Hardening Tricalcium Phosphate Cement, *Int. J. Mol. Sci.*, 2019, **20**(2), 391.

45 A. Kramida, Y. U. Ralchenko and J. Reader, NIST ASD Team, *NIST Atomic Spectra Database*, 2018, available from: https://www.nist.gov/pml/atomic-spectra-database.

46 D. W. Hahn and N. Omenetto, Laser-Induced Breakdown Spectroscopy (LIBS), Part II: Review of Instrumental and Methodological Approaches to Material Analysis and Applications to Different Fields, *Appl. Spectrosc.*, 2012, **66**(4), 347–419.

47 X. Bai, Q. Ma, M. Perrier, V. Motto-Ros, D. Sabourdy, L. Nguyen, *et al.*, Experimental study of laser-induced plasma: Influence of laser fluence and pulse duration, *Spectrochim. Acta Part B At. Spectrosc.*, 2013, **87**, 27–35.

48 Q. Ma, V. Motto-Ros, F. Laye, J. Yu, W. Lei, X. Bai, *et al.*, Ultraviolet versus infrared: Effects of ablation laser wavelength on the expansion of laser-induced plasma into one-atmosphere argon gas, *J. Appl. Phys.*, 2012, **111**(5), 053301.

49 M. A. Kasem, J. J. Gonzalez, R. E. Russo and M. A. Harith, Effect of the wavelength on laser induced breakdown spectrometric analysis of archaeological bone, *Spectrochim. Acta Part B At. Spectrosc.*, 2014, **101**, 26–31.

50 X. Li, Z. Wang, Y. Fu, Z. Li and W. Ni, Wavelength Dependence in the Analysis of Carbon Content in Coal by Nanosecond 266 nm and 1064 nm Laser Induced Breakdown Spectroscopy, *Plasma Sci. Technol.*, 2015, **17**(8), 621–624.

51 O. Samek, D. C. S. Beddows, H. H. Telle, G. W. Morris, M. Liska and J. Kaiser, Quantitative analysis of trace metal accumulation in teeth using laser-induced breakdown spectroscopy, *Appl. Phys. A: Mater. Sci. Process.*, 1999, **69**(S1), S179–S182.

52 H. J. Naser and T. K. Hamad, Quantitative Analysis of heavy metals in gallstone Using LIBS, *J. Phys. Conf.*, 2021, **1963**(1), 012089.